Mon. Not. R. Astron. Soc. **269**, 37–51 (1994)

0319 − 454: an FR II giant radio galaxy with twin jets

Lakshmi Saripalli,[1] Ravi Subrahmanyan[2]★ and Richard W. Hunstead[3]

[1] *Radioastronomisches Institut, University of Bonn, Auf dem Hügel 71, D-53121 Bonn 1, Germany*
[2] *Institut für Astrophysik, University of Bonn, Auf dem Hügel 71, D-53121 Bonn 1, Germany*
[3] *School of Physics, University of Sydney, NSW 2006, Australia*

Accepted 1994 January 28. Received 1994 January 27; in original form 1993 November 24

ABSTRACT

We present radio images of the edge-brightened giant radio galaxy 0319 − 454 made with the Australia Telescope at frequencies 1.5, 2.4 and 4.8 GHz. The observations show a jet and a counterjet out to exceptional distances of 380 and 590 kpc, respectively, from the radio core. 0319 − 454 is therefore one of only three powerful radio galaxies observed to date to have twin quasi-continuous jets. The NE lobe of the double radio structure has an extremely rare configuration of five compact hotspots that may be classified into a primary and a cluster of four secondaries. Optical imaging of the parent galaxy reveals a prominent, warped dust lane, and a highly disturbed structure that is indicative of past merger activity.

Key words: galaxies: active – galaxies: individual: 0319 − 454 – galaxies: jets – radio continuum: galaxies.

1 INTRODUCTION

The transport of energy from active galactic nuclei to the extended radio-luminous lobes seen in radio galaxies and quasars is believed to occur as bulk kinetic motion of material in collimated beams. The ubiquitous detection of jets in low-luminosity radio galaxies and quasars validates this 'beam' model. However, jets are rare in powerful radio galaxies (PRGs) exhibiting an edge-brightened structure, and the detected jets in PRGs and quasars are almost always one-sided.

The beams in powerful radio sources with an edge-brightened structure (FR II, Fanaroff & Riley 1974) are generally believed to be supersonic and the energy is transported with minimal losses, whereas the low-luminosity sources (FR I) have lossy, subsonic beams (Williams & Gull 1984; Bicknell 1985). The visibility of the beam in FR I sources is then inferred to be a consequence of the inefficient flow, and their rarity in powerful radio galaxies (FR II) is attributed to the highly efficient flow. However, jets are frequently observed in quasars, although they are powerful FR II radio sources. Various observed properties of quasars suggest that the relativistic beams in them emerge along an axis that is close to the line of sight (Barthel 1989). The Doppler boosting of the jet emission on the side oriented towards the observer would consequently enhance the visibility of quasar jets and also cause them to be apparently one-sided. In the absence of similar evidence for strong Doppler beaming effects in PRGs, the asymmetry seen in their jets could be interpreted as implying one-sidedness in their beams and the symmetry in their extended radio structures (lobes and hotspots) inferred to be due to alternations in the direction of emergence (Rudnick & Edgar 1984). On the other hand, the observations of a split [O III] line on the side of the invisible jet in 3C 120 (Axon et al. 1989) are suggestive of beams being intrinsically double-sided, and therefore it appears that Doppler beaming effects are probably important in the PRGs as well.

The unified models for radio galaxies and quasars (Barthel 1989, 1990) seek to attribute their morphological differences to orientation effects alone, and the PRGs are proposed to be those sources where the observable effects of Doppler beaming anisotropy are less pronounced than in quasars. This model is attractive because, if quasars are the sources where the beams are directed close to the line of sight, PRGs are the only viable candidates for sources where the beaming angle is larger (see Browne & Jackson 1990 for a discussion of the merits and demerits of this scheme). In this unified model, the PRGs would be expected to show fewer and less prominent jets than quasars, and smaller values of jet-to-counterjet flux density ratio. This prediction has been tested through sensitive observations attempting to detect counterjets in PRGs (Bridle 1990, 1992; Fernini et al. 1993), and it appears that, although these sources never show jet-to-counterjet ratios close to unity, the values are always less than for quasars. It may be noted here that,

★ On leave from the Tata Institute of Fundamental Research, Poona University Campus, Post Bag 3, Pune 411007, India.

although the kpc-scale jets in PRGs are assumed to be propagating with relativistic velocities for the Doppler beaming effects to be manifest, the Lorentz factor Γ is not believed to be very large since the Doppler effect would then severely suppress the observable emission from even the approaching beam (because the emission is beamed into a cone of angle $1/\Gamma$ which could exclude the observer for large Γ).

To date, detections of emission associated with the beam on the counterjet side of FR II sources have, almost without exception, been only knots which are often elongated in the direction of the hypothetical beam (Bridle 1990). This emission is likely due to local disturbances in the path of the beam, whereas the emissivity detected in continuous jets is believed to represent general inefficiency in the beam propagation. Estimates of jet-to-counterjet flux density ratios derived from images detecting only knots associated with the counterjet are therefore better interpreted as a lower limit. While counterjet knots are certainly suggestive of the presence of beamed emission, a study of the intrinsic properties of beams on both sides is facilitated by detections of continuous or quasi-continuous jets on both sides.

The radio galaxies with linear sizes exceeding 1.5 Mpc (we adopt a Hubble constant of 50 km s^{-1} Mpc^{-1} in this paper) form the class of giant radio galaxies (GRGs, Saripalli et al. 1986). They are more than 10 times the typical size of an FR II radio galaxy, and they are observed to have only narrow optical emission lines in their nuclear spectra. Both properties suggest that the radio axes of these sources make small angles to the plane of the sky. Jets (on one side) have been detected in many GRGs. The relativistic beaming hypothesis predicts that these giant powerful radio galaxies are most likely to have small jet-to-counterjet flux density ratios, and therefore high-resolution observations of the beams in these sources could help to clarify the hypothesis.

The extended radio source 0319−454 was tentatively identified with a $z = 0.0633$ peculiar dust-laned galaxy, and thereby inferred to be a powerful and giant radio galaxy of linear size 2.54 Mpc (Jones 1989). The radio structure is of FR II type, with edge-brightened radio lobes. Our radio observations of 0319−454 have detected a quasi-continuous jet and counterjet. In the following sections, we present our radio and optical observations of various unusual features in this giant source, and discuss the origins of these peculiarities.

2 OBSERVATIONS AND DATA ANALYSIS

2.1 Radio imaging at 1.5, 2.4 and 4.8 GHz

0319−454 was observed in several array configurations of the six-antenna east–west array of the Australia Telescope Compact Array (ATCA, see The Australia Telescope 1992) during the period 1991 September to 1992 January. Observations at 2368 MHz were made with four configurations (3.0A, 3.0B, 3.0C and 3.0D), selected to give a uniform coverage of baseline lengths up to 3 km, and an additional compact 1.5D configuration to measure low spatial frequencies. Visibility data at 1472 MHz were obtained simultaneously during the observations in the 3.0B, 3.0D and 1.5D configurations. These observations were made with the antenna pointing and field centre placed roughly at the centre of the radio structure, but offset from the radio axis. Observations of the northern lobe were made separately at 4796 MHz in a single 1.5D-array configuration. All the observations were made over 12-h periods in order to obtain full azimuthal coverage of visibility measurements in the Fourier plane. The continuum observations were made in a multichannel mode covering a total bandwidth of 128 MHz at each frequency. 0319−454 has an angular size of 25.6 arcmin (Jones 1989), and the antennas have primary beam half-power widths of about 35, 22 and 11 arcmin at 1472, 2368 and 4796 MHz, respectively. We expect the imaging to reproduce extended structures up to about 4- and 8-arcmin scales at 2368 and 1472 MHz, respectively.

Standard NRAO Astronomical Image Processing (AIPS) software was used for the data reduction. Frequent observations of the unresolved source 0332−403 were used to calibrate the bandpass responses and time variations in complex gains of the interferometer elements. The overall flux density scale was set separately in each observation by bootstrapping the calibrator visibility amplitudes to observations of PKS 1934−638. The flux density of this primary calibrator was adopted to be 14.90, 11.97 and 6.34 Jy at 1472, 2368 and 4796 MHz, respectively.

At 4796 MHz the multichannel continuum visibilities were averaged to form a single continuum band covering 84 MHz. The visibility phases were self-calibrated in two passes, and the data were imaged and deconvolved using the AIPS routine MX. The calibrated multichannel visibilities at 1472 and 2368 MHz were gridded together and then imaged using the AIPS routine MX to avoid bandwidth smearing effects. The extended and low-surface-brightness components in the resulting image were deconvolved using the maximum-entropy-method deconvolution routine VTESS. The CLEAN components corresponding to the point-like sources and the VTESS image of the extended emission were convolved with a Gaussian restoring beam and added to the residuals to form the final deconvolved images at the two frequencies. Because the residuals were not deconvolved, the half-power sizes of these restoring beams were chosen to be the same as the original synthesized beams.

The 1472-MHz image of 0319−454, smoothed to a resolution of 40-arcsec FWHM, is shown in Fig. 1, and displays the overall extended structure of the radio source; this compares well with the 843-MHz image of Jones (1989). Higher resolution structure in the NE lobe at 2368 MHz is displayed in Fig. 2(a) as a contour representation, and in Fig. 2(b) as a grey-scale to display low-contrast features not apparent in the contour plot. The 4796-MHz image of the hotspot structure in the NE lobe is shown in Fig. 3. Images of the region around the core of the radio source are shown in Figs 4(a) and (b) at frequencies 2368 and 1472 MHz, respectively. The structure in the SW lobe is shown in Fig. 5 as a contour representation of the 1472-MHz image. All the images have been corrected for the attenuation due to the primary beams.

2.2 Radio structure of 0319−454

The radio galaxy 0319−454 has an FR II-type, edge-brightened structure with a compact unresolved core (referred to as component P in the figures) and well-resolved NE and SW lobes. The source is very asymmetric in the core–lobe separation and in lobe structure. The total flux density of the

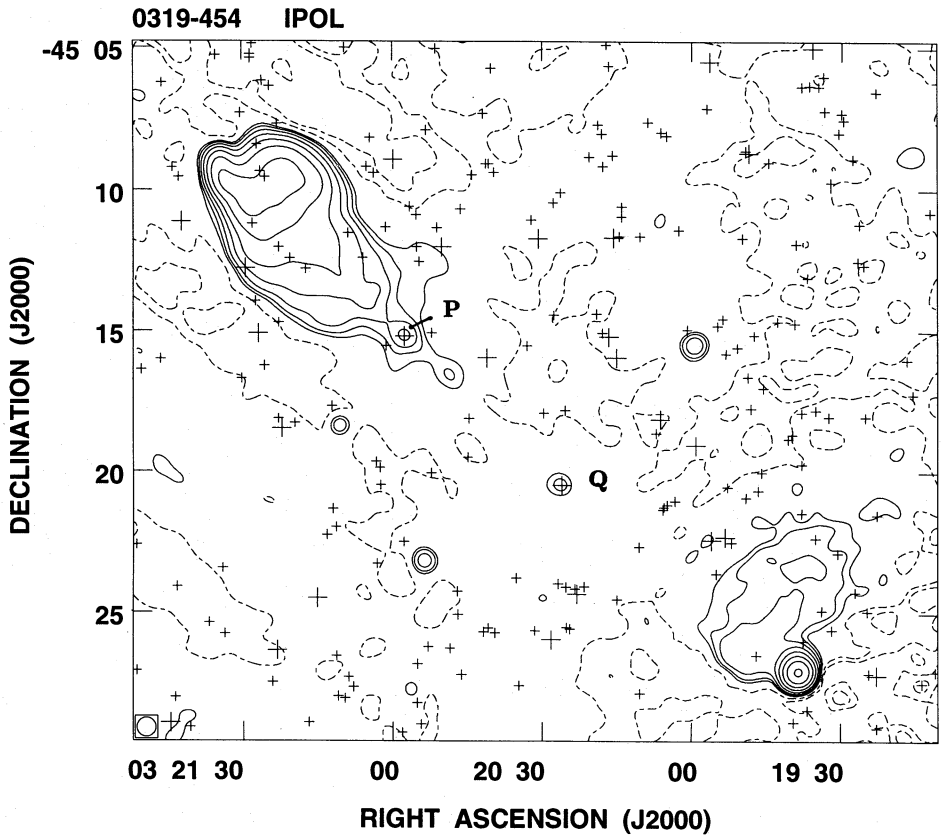

Figure 1. 1472-MHz image of 0319−454, smoothed to a resolution of 40-arcsec FWHM. The beam half-power width is indicated by the circle in the lower left-hand corner. Contours are at 1 mJy beam^{-1} × (−8, −4, −2, 2, 4, 8, 16, 32, 64, 128, 256). Positions of optical galaxies in the field are indicated by crosses; larger symbols indicate galaxies within ±3 mag of the host galaxy (marked P), smaller symbols indicate fainter galaxies. Q indicates the position of a possible edge-on spiral galaxy.

source is measured to be 3.83 and 2.04 Jy at 1472 and 2368 MHz, respectively (after subtracting contributions from unrelated sources in the field). A comparison with previous flux density measurements of the source summarized in Jones (1989), together with our revised estimate of 5.35 Jy (4.64 Jy in the NE component and 0.71 Jy in the SW component) at 843 MHz, indicates that the overall spectrum of the source is probably curved: mean $\alpha \approx 0.75$ ($S_\nu \propto \nu^{-\alpha}$) near 1 GHz, with a flattening below 400 MHz and a steepening above 2 GHz. Our imaging does not seem to have missed any significant flux density at 1472 MHz, although the image at 2368 MHz could have up to 30 per cent missing flux density (after correcting for attenuation due to the primary beam).

The ATCA images have revealed a quasi-continuous jet towards the NE (components marked J1 and J2) and a counterjet towards the SW (components marked CJ1, CJ2, CJ3 and CJ4). All these jet and counterjet components are detected at both 1472 and 2368 MHz (Figs 4a and b), and at levels exceeding 4 times the rms noise in the images. The main NE jet is traced over a distance of 3.8 arcmin from the core and well into the NE lobe. The quasi-continuous counterjet is detected out to a distance of 6 arcmin from the core. However, this is only about one-third of the distance to the SW hotspot and associated lobe emission.

The NE lobe is well resolved into multiple hotspots (marked HS1 to HS5 in Fig. 3) and a very diffuse lobe that extends back from the hotspots at least as far as the core. The SW lobe has a single hotspot component (marked SHS in Fig. 5), whose brightness dominates the source. Since this bright component lies in the vicinity of the half-power points of the telescope primary beams at 2368 and at 1472 MHz, errors in the images are dominated by residual sidelobes which are probably caused by pointing errors in the antenna elements. As a consequence, emission close to the SW hotspot is not well represented in the images. Nevertheless, it is worth noting that the structure of the diffuse emission in this region at 1472 MHz is very similar to that seen at 843 MHz by Jones (1989).

2.3 Optical imaging in *R* and *B* bands

Optical images of the galaxy at the position of the radio core were obtained in *R* and *B* bands at the prime focus of the Anglo-Australian Telescope (AAT) as service observations. The exposures were 300 s, and the detector was a Tektronix 1024^2 CCD with a pixel size of 0.39 arcsec, giving a field of view of 6.65×6.65 arcmin^2. The images have been bias-subtracted and flat-fielded. The coordinate frames for the two images were independently determined using stars in the fields, in order to bring the two CCD images into accurate registration (within 0.5 arcsec) with respect to each other and with the radio images. Based on 36 standards in several E-

region fields observed on the same night, the photometric calibration for the B and R images of 0319−454 was determined to be

$$R = 28.68 + 0.015(B-R) - 2.5\log_{10}(\text{counts})\ \text{mag arcsec}^{-2} \quad (1a)$$

and

$$B = 28.71 + 0.089(B-R) - 2.5\log_{10}(\text{counts})\ \text{mag arcsec}^{-2}. \quad (1b)$$

The sky brightness was measured to be 20.9 and 22.4 mag arcsec^{-2} in R and B, respectively, after averaging the background counts in image pixels in several source-free regions. The seeing was about 2.0 arcsec in R and 2.45 arcsec in B.

Contour representations of the parent galaxy in R and B are shown in Figs 6(a) and (b), respectively, in counts which may be converted to R and B magnitudes using (1). The background has been subtracted, and the images have been convolved with Gaussians to broaden the seeing disc to a uniform FWHM of 3 arcsec in both bands. The radio axis and the warped dust lane are indicated in Fig. 6(b), and the position of the peak of the radio core is indicated by a cross.

3 THE CENTRAL OBJECT

The compact radio source observed at the position marked P in Fig. 1 coincides with the optical identification proposed by Jones (1989), and almost certainly locates the position of the central engine of the radio galaxy. The low-resolution spectrum in the visible (Jones 1989), despite poor signal-to-noise ratio, shows possible [O III] emission and weak but broad Hα emission, along with the absorption features and continuum inflections of an elliptical galaxy. In addition, a recent K-band echelle spectrum of the nucleus, obtained as a service observation with IRIS on the AAT, shows prominent Paschen α 1.8751-μm emission at 2.00 μm. These data all confirm the presence of an active nucleus, but one which is heavily obscured.

The other possible identification for the radio core is the source marked Q in Fig. 1 that lies midway between the two radio lobes and on the ridge line defined by the jet-like fea-

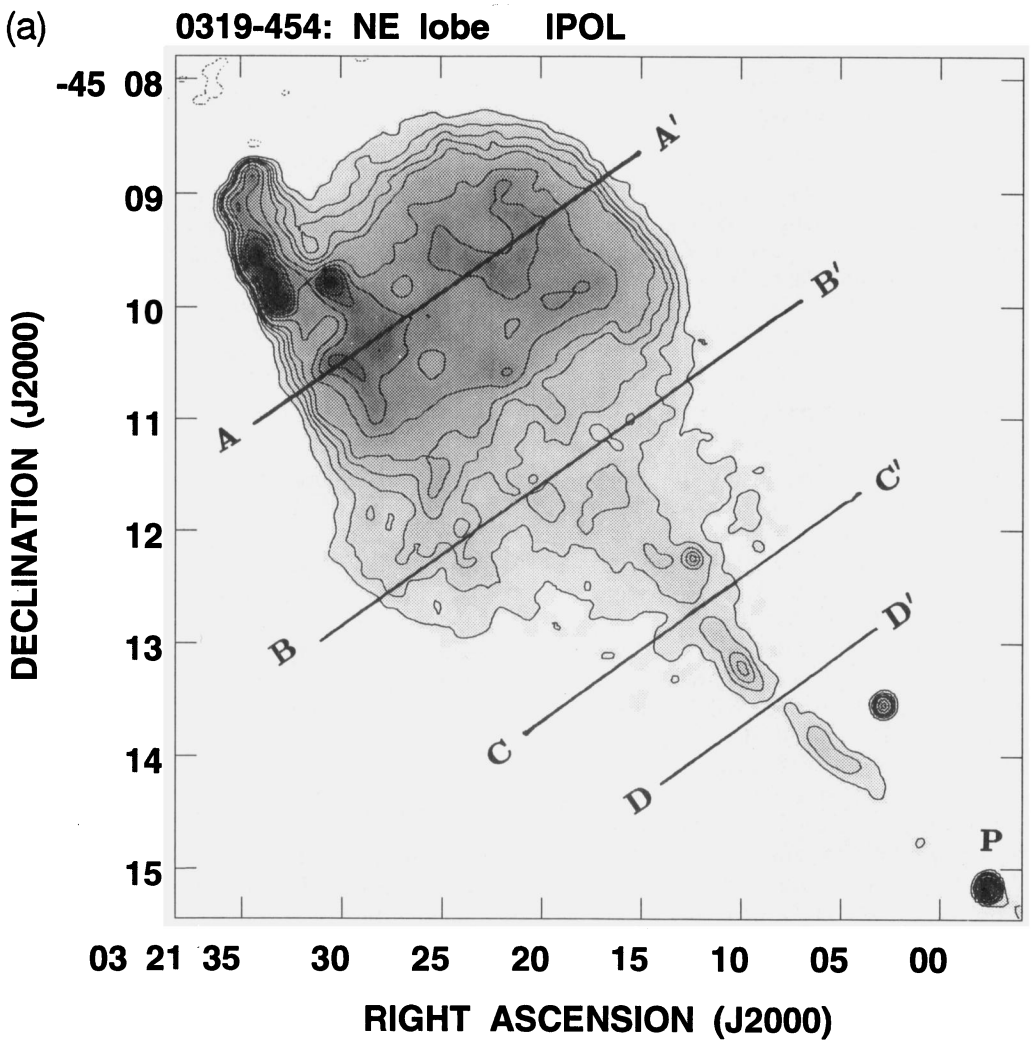

Figure 2. 2368-MHz image of the NE lobe of 0319−454 made with a resolution 8.14×7.32 arcsec^2 FWHM at a position angle of 5°.7. (a) Contour representation with levels drawn at 0.1 mJy beam^{-1} × (−4, 4, 8, 12, 16, 20, 30, 40, 50, 60, 80, 100). Lobe pressures are derived in Section 6 along the four slices indicated. The core component is marked P. (b) Grey-scale representation of intensities in the range 2–6 mJy beam^{-1}, showing the filamentary structure in the NE lobe. The direction towards the core is also indicated.

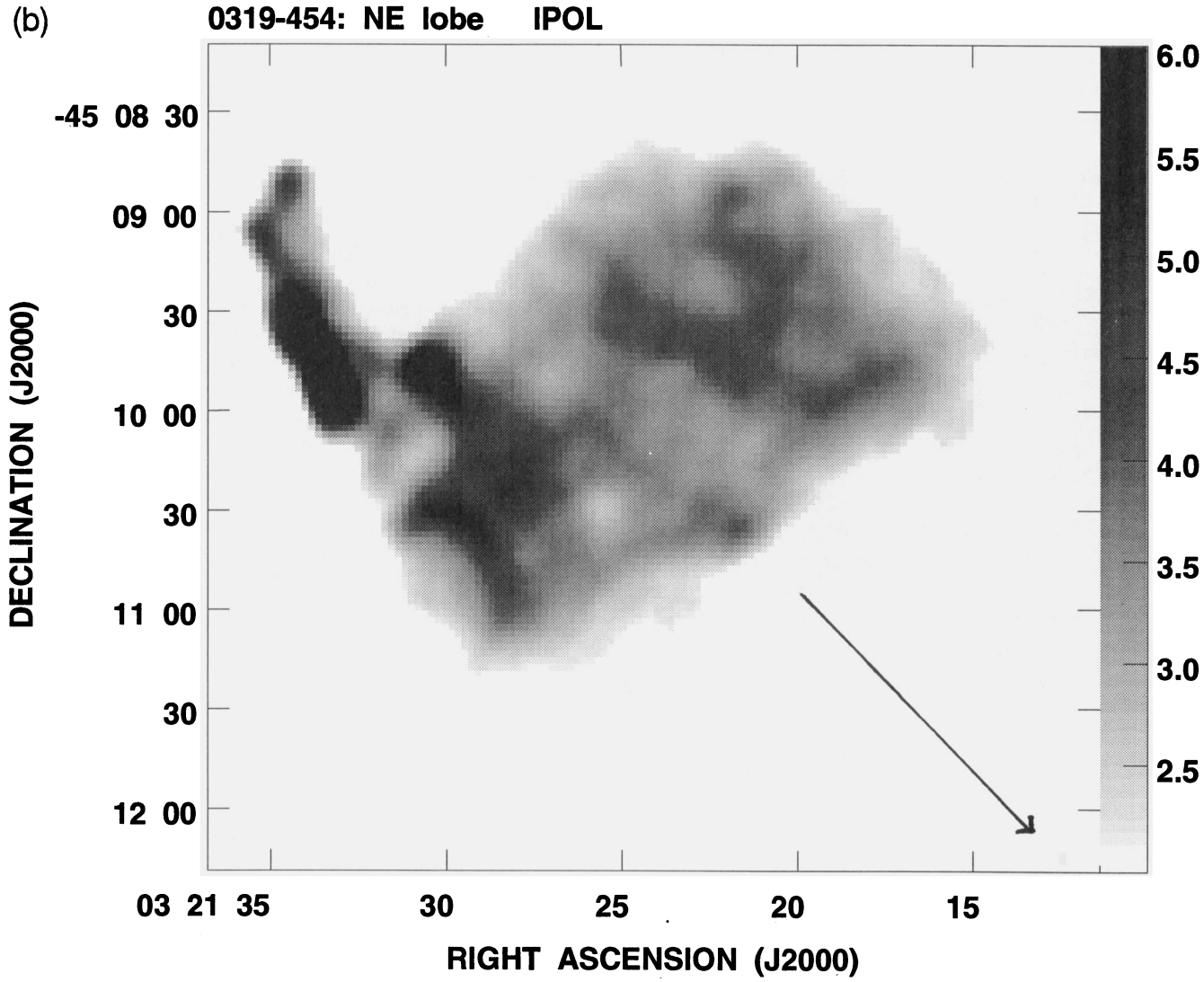

Figure 2 - *continued*

ture. However, this component has a steep spectral index of $\alpha = 0.8$ between 1.5 and 2.4 GHz, is strongly elongated (with a deconvolved size of about 6×2 arcsec^2), and is identified with what appears to be an edge-on spiral galaxy (Jones 1989). Moreover, the radio axis of Q and the major axis of the galaxy are aligned. These factors suggest that Q is unrelated to 0319−454.

3.1 The radio core: radio properties

The radio core is slightly resolved by our 8-arcsec resolution radio imaging, and we estimate its size to be $\lesssim 2$ arcsec (see Jones et al. 1994 for a long-baseline interferometer observation of the core). The spectral index is flat between 1.5 and 2.4 GHz ($\alpha = 0.2$), and becomes even flatter beyond 2.4 GHz. We list the core flux densities in Table 1. The fractional flux in the radio core (defined as the ratio of the core flux density at 5 GHz to the total flux density at 0.408 GHz) and the core power at 5 GHz are 0.14 per cent and 2.5×10^{23} W Hz^{-1}, respectively. These values are similar to the corresponding quantities observed in other giant radio galaxies (Saripalli & Gopal-Krishna 1987; Saripalli 1988). The core prominence and radio luminosity in 0319−454 are also similar to those of smaller-sized FR II radio galaxies at the same redshift.

3.2 The parent galaxy: optical properties

0319−454 is located well away from the Galactic plane ($l = 254\overset{\circ}{.}5$, $b = -55\overset{\circ}{.}2$), and the interstellar extinction, $E(B-V)$, is less than 0.015 mag (Burstein & Heiles 1982). We expect the corrections to the observed optical magnitudes of the parent galaxy to be less than 0.1 mag in the V band, and consequently we have not applied any Galactic extinction corrections.

The parent galaxy, ESO 248−G10, has an extremely large size, extending 100 and 85 kpc along the major and minor axes of the $R_{24.5}$ (approximately the same as the V_{25}) mag arcsec^{-2} contour. By integrating the intensities to the $R = 25$ mag arcsec^{-2} isophote, we see that the galaxy has an appar-

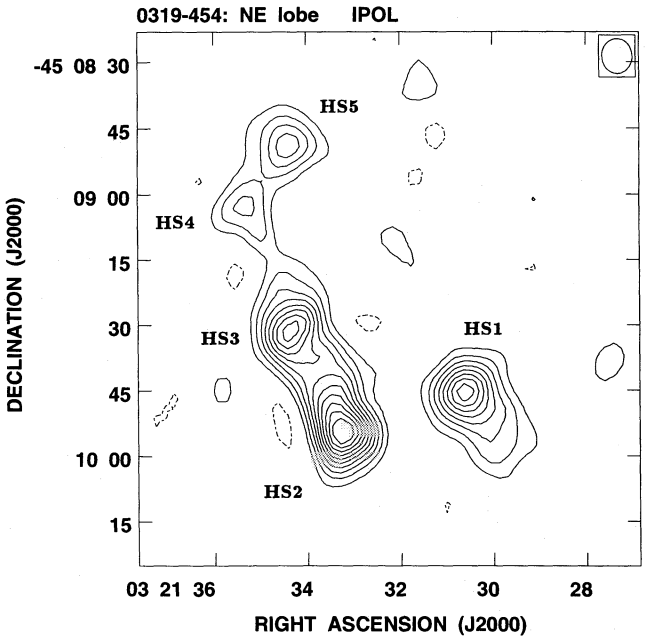

Figure 3. 4796-MHz image of the five hotspots in the NE lobe. Resolution: 7.94×6.90 arcsec^2 FWHM. The beam half-power width is indicated by the ellipse in the upper right-hand corner. Contours are at 0.1 mJy beam$^{-1} \times (-5, 5, 10, 15, 20, 25, 30, 35, 40, 45, 50)$. The five emission components are marked HS1, HS2, HS3, HS4 and HS5.

ent magnitude of $m_R = 14.2$. The absolute magnitude, $M_R = -23.7$, is close to the median luminosity of PRGs. A prominent dust lane bisects the galaxy image and strongly disturbs the brightness contours in the inner parts of the galaxy. The luminosity profile away from the central band of obscuration and in a direction perpendicular to this dust lane generally follows a de Vaucouleurs $r^{1/4}$ law between 13 and 40 kpc from the nucleus. A fit to this $r^{1/4}$ law gives the effective radius of the galaxy to be $r_e = 10$ kpc, and the brightness at this radius is $\mu_e = 21.0$ R mag arcsec^{-2}. These parameters classify ESO 248–G10 as a luminous (peculiar) giant elliptical galaxy (Tonry 1987). The galaxy also falls within the parameter space delineated by PRGs and brightest cluster galaxies in the μ_e–r_e relationship. However, it is relatively centrally condensed (small r_e) and has a large R_{25} size.

Away from this dust lane, the isophotes clearly indicate significant morphological deviations from elliptical symmetry at the relatively high surface brightness of 22.3 (23.7) mag arcsec^{-2} in $R(B)$. The isophotes have a boxy appearance overall at this brightness and appear very disturbed, indicating the presence of complex small-scale structure. A plume with a surface brightness of between 24.6 and 25.2 mag arcsec^{-2} in R is seen extending from the main body of the elliptical galaxy for 30 kpc towards the north-west. An oppositely directed extension with an even higher surface brightness is also seen towards the south-east in both the R and B images.

An image of the galaxy in $B-R$, formed by dividing the smoothed R and B images, is shown in Fig. 6(c). This image clearly shows the increased reddening along the broad dust lane and, in particular, towards the nuclear region. The mean colour towards the main body of the galaxy is 1.65 in $B-R$. Assuming a colour of 1.55 in $B-R$ for a giant elliptical at redshift $z=0$ and passive evolution, the galaxy at redshift $z=0.0633$ is expected to have $B-R > 1.74$. Therefore the main body of ESO 248–G10 is overall at least 0.1 mag bluer in $B-R$ than a giant elliptical at its redshift. The main body of the galaxy also shows significant small-scale colour variations over the range 1.5 to 1.8 in $B-R$, suggesting spatial variations in the stellar populations. The $B-R$ image shows a prominent and extended blue patch about 10 arcsec (17 kpc) to the east of the nucleus, with a colour $B-R=1.3$, i.e. 0.3 mag bluer than the surrounding material. Several PRGs have been observed to have secondary nuclei and such straddling blue patches of emission (see, for example, Smith & Heckman 1989), which are found to be mostly stellar in content. A less prominent red object (with $B-R=1.8$) is also seen 15 arcsec to the south (and slightly west) of the nucleus. The extension seen to the south-east in the R- and B-band images appears to be bluer than the surrounding material. The colour in the north-west extension and plume, however, cannot be reliably determined, because in the blue image this region is influenced by the presence of scattered light from a very bright star to the north of the galaxy and outside the CCD field of view.

Near-infrared images of the parent galaxy in H, J and K' bands were obtained during commissioning time with the IRIS infrared facility at the AAT (David Allen, private communication). These images showed an unresolved source at the nucleus of the galaxy. The red feature seen in the $B-R$ image 15 arcsec to the south of the nucleus is also seen on the H- and J-band images, but is not obvious on the K' image.

The dust lane has a width of about 6 arcsec (10 kpc) and extends 45 arcsec (75 kpc) across the galaxy. The band of extinction is observed to have an integral-sign shape, suggesting that the dust is distributed in a warped disc. The central part of the dust lane is seen to be aligned along the major axis of the inner isophotes, and therefore we classify ESO 248–G10 as a major-axis dust-lane elliptical galaxy. The peak of the reddening (as seen on the $B-R$ image) is located to the north of the peaks in the R- and B-band images, indicating that the normal to the dust disc is inclined away from the sky plane to the north. The maximum reddening observed due to the dust lane corresponds to an $E(B-R)=0.83$.

The position angles of the best-fitting ellipses show a large twist through about 40° in going from the inner to the outer isophotes. The minor axis of the galaxy (defined as the minor axis of the inner bright isophotes) is at a position angle of 17°, and this is also the direction of the normal to the dust lane. Surprisingly, the radio axis close to the core has a position angle of $\approx 51°$ and is not aligned with the galaxy minor axis or the normal to the dust lane (misalignment of 34°; see Fig. 6b). However, this radio axis (inner) is aligned with the minor axis of the outer isophotes, and is approximately orthogonal to the direction defined by the plume to the NW and blue extension observed to the SE.

The position of the peak of the radio core is observed to be offset 2 arcsec from the peak in the optical R-band image (Table 1), and we do not believe that this is due to inaccuracies in aligning the radio and optical reference frames. There could, however, be errors in determining the position of the galactic nucleus due to the extinction in the dust lane.

3.3 Merger origin

Interactions between galaxies are generally expected to result in morphological peculiarities like tails, plumes (Toomre & Toomre 1972) and shell-like structures (Malin & Carter 1980; Quinn 1984), bluer colours in the main body of the galaxies due to induced bursts of star formation (Larson & Tinsley 1978), and higher luminosities in the infrared and radio (Lonsdale et al. 1984). The presence of disturbed, peculiar optical structures and blue colours in a large fraction of PRGs and quasars (Heckman et al. 1986; Smith & Heckman 1989; Stockton 1990) indicates that interactions can also trigger activity in the nucleus. The H I rings, emission-line gas discs and dust in the major- and minor-axis dust-lane elliptical galaxies are believed to have an external origin (Bertola 1987; Knapp 1987; Sadler 1987; Bertola et al. 1988) and are therefore a signature of a past encounter.

In ESO 248-G10 we observe (1) a warped dust lane oriented along the major axis of the elliptical galaxy; (2) very disturbed and boxy isophotes; (3) the colour of the main body to be overall bluer than in giant elliptical galaxies at the same redshift; (4) significant non-uniformity in colours: a blue extended patch of emission located about 17 kpc east of the nucleus and a red compact object south of the nucleus; (5) a plume extending about 30 kpc to the NW and an extension towards the SE which is bluer than the surrounding material. The galaxy is also extraordinarily large ($\gtrsim 100$ kpc) and luminous. ESO 248-G10 is possibly a product of a merger, with the dust accreted as a result.

The galaxy is suggested as being in a cluster (Holmberg et al. 1978), but our optical images suggest that the cluster is poor. This is consistent with the finding that merger products that are PRGs lie in regions of low galaxy density (Smith & Heckman 1989).

4 THE JET AND COUNTERJET

The two jets detected in 0319−454 (Figs 4a and b) to the NE and SW of the core appear to be quasi-continuous, and consist of several elongated knots. The rare detection of jet

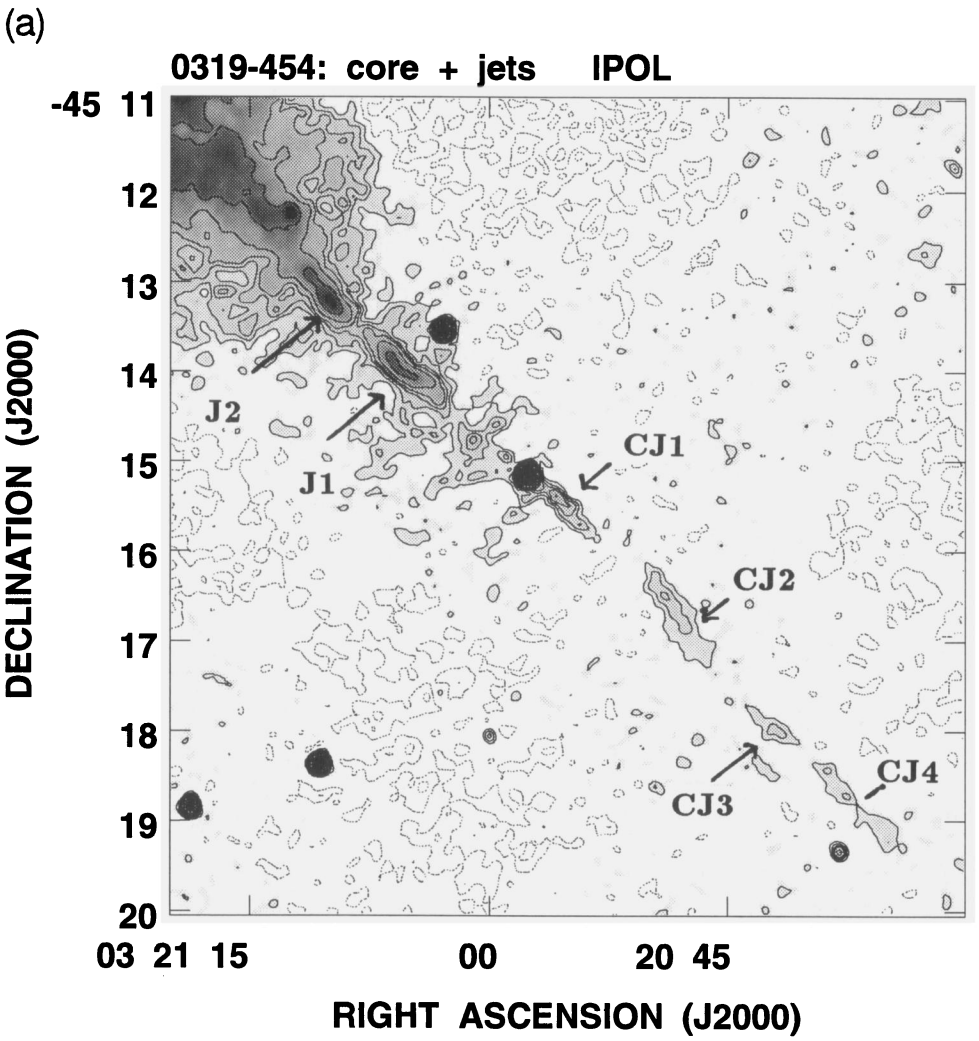

Figure 4. The jet and counterjet in 0319−454 shown as superpositions of contours and grey-scale representations. The jet components are marked J1 and J2, counterjet components are marked CJ1, CJ2, CJ3 and CJ4. (a) 2368-MHz image made with a resolution of 8.14 × 7.32 arcsec^2 FWHM at a position angle of 5°.7. Contours are at 0.1 mJy beam^{-1} × (−3, −2, −1, 1, 2, 3, 4, 6, 10). (b) 1472-MHz image made with a resolution of 9.59 × 8.60 arcsec^2 FWHM at a position angle of 10°.8. Contours are at 0.15 mJy beam^{-1} × (−2, −1, 1, 2, 4, 6, 9, 12, 15, 20, 30).

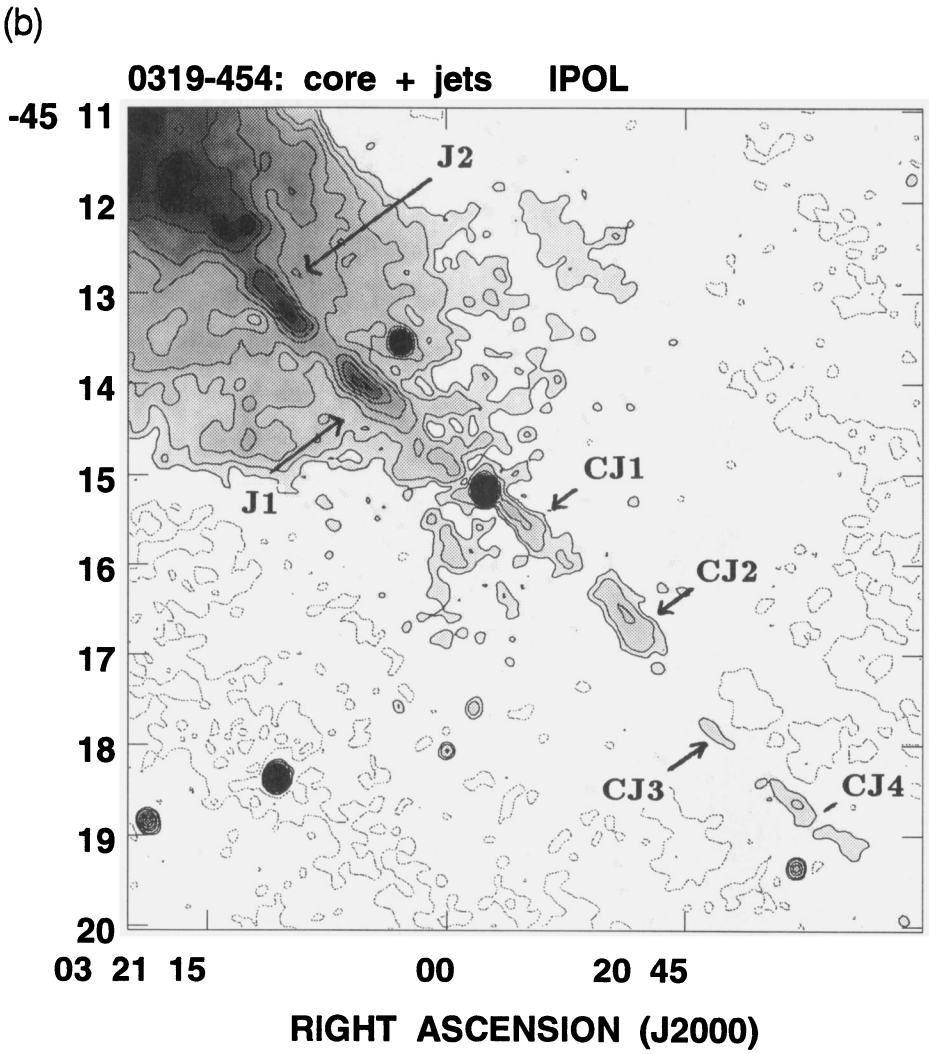

Figure 4 – *continued*

and counterjet in this distinctly edge-brightened source in our images with moderate (≈ 100) dynamic range might be an observational selection effect due to the similarity between the jet widths and resolution, and the absence of enveloping diffuse emission around the weaker counterjet. Sources like 0319−454 which are close to the FR I–II luminosity boundary might have jet physics intermediate between the two categories, and this may also favour the detection of twin jets.

The knots J1, J2 and CJ1, CJ2 each meet Bridle's (1984) criterion for a genuine jet, each having a length of at least four times their width. We refer to the NE side of the core, where the jet-like features appear to be brighter, as the 'jet-side' and to the SW side of the core as the 'counterjet-side'. The jet is traced to a distance of 380 kpc (40 per cent of the distance to the NE hotspots) from the core (Fig. 1), and appears to be enveloped in backflow material from the NE lobe throughout its length (Leahy & Williams 1984; Williams & Gull 1984). Beyond 380 kpc, the jet is not distinguished from the lobe. The brightness of the jet knots J1 and J2 increases away from the core. The counterjet is traced to 590 kpc (one-third of the distance to the SW hotspot) from the core, and the brightness of the detected knots CJ1 to CJ4 decreases away from the core. The counterjet may not have been detected in our imaging over the remaining two-thirds of the distance to the SW hotspot because of its low brightness compared with the image noise. Backflow from the SW lobe appears to be deflected to the north, and the counterjet is probably in contact with the intergalactic medium over most of its length.

The detected flux densities in the jet and counterjet at 2368 MHz are 22 and 9 mJy, respectively, corresponding to 1 and 0.4 per cent of the total source emission. The jet-to-counterjet intensity ratio is 3.7 when measured over a fixed angular distance of 3.7 arcmin. The relatively low prominence of the jets and the observed ratio of the intensities in the two jets are both characteristic of PRGs (e.g. Cyg-A, Bridle 1986, 1990). The contrast in the jet, defined as the ratio of the peak brightness in the detected knots to the minimum intensity in the interknot region, is $\gtrsim 4$. The counterjet has a contrast exceeding 3. The jets in 0319−454 are not smooth features, and this lack of smoothness in the observed jets is also a characteristic of the PRGs. The deconvolved width of the jet is fairly constant at 10 arcsec (17 kpc) over the knots J1 and

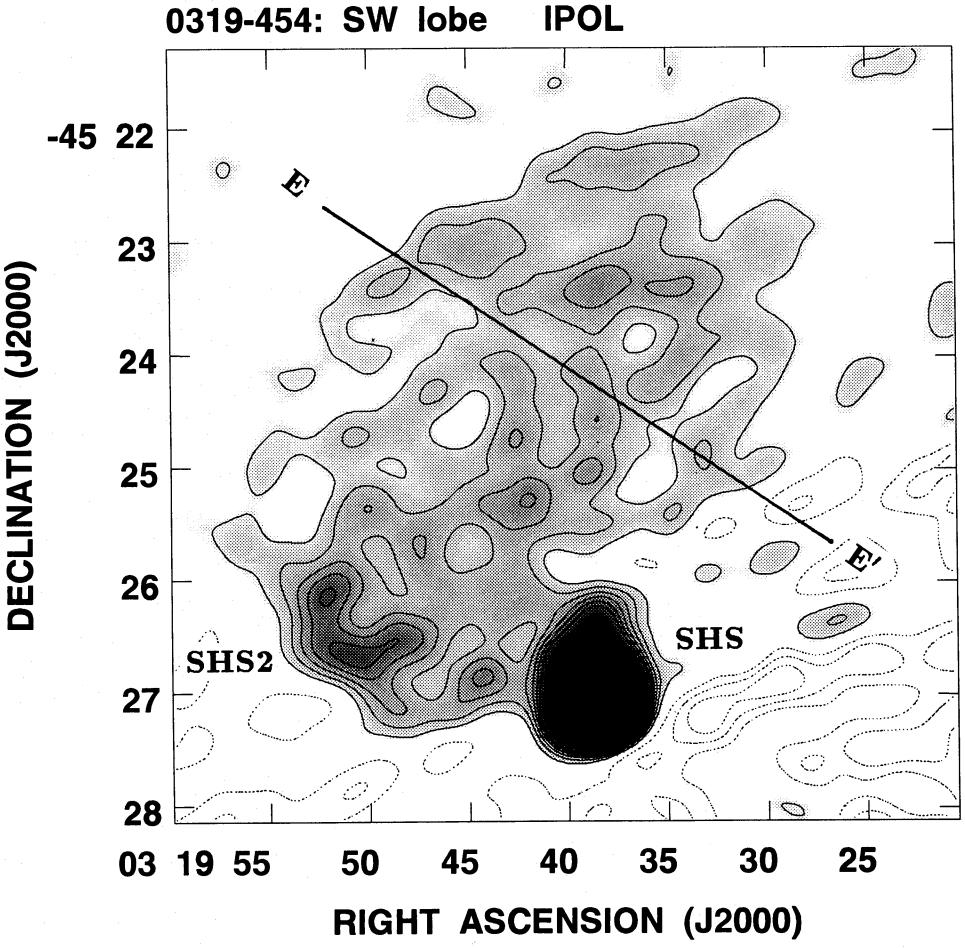

Figure 5. 1472-MHz image of the SW lobe smoothed to a resolution of 20-arcsec FWHM. Contours are at 1 mJy beam^{-1} × (−3, −2, −1, 1, 2, 3, 4, 5, 6, 8, 10). Grey-scale range: 0.5–10 mJy beam^{-1}. Lobe pressure is derived in Section 6 along the slice indicated.

J2. The counterjet segment CJ1, which is closest to the core, is essentially unresolved (< 8 arcsec) transverse to its length. Further away, the segment CJ2 is resolved and has a width of about 10–14 arcsec (17–22 kpc). Overall, the counterjet appears to flare over the length defined by segments CJ1 and CJ2.

The jet component J1 shows a small-scale wiggle with a wavelength of about 80 kpc (see Fig. 4a), and the elongated segment J2 has a position angle that is misaligned with the overall radio axis. The highly elongated counterjet components CJ1 and CJ2 also appear to be significantly misaligned with the overall radio axis, and could be interpreted as due to an overall wiggle in the counterjet, with a wavelength of about 170 kpc, which exists for the first 300 kpc of its path. However, the detected counterjet knots CJ3 and CJ4 that lie further from the core are collinear with the core and the jet segments. The lack of inversion symmetry in the oscillations seen to the NE and SW of the core suggests that precession in the ejection axis may not be the dominant cause for the misalignments. The asymmetric oscillations may arise due to instabilities in the propagation of the beam through the differing environments on the jet and counterjet sides (but see Section 5.2 for an alternative interpretation for the misalignment in counterjet segments). The wavelength of the oscillations due to Kelvin–Helmholtz instabilities (Hardee 1983) is inversely proportional to the density contrast between the jet and ambient medium ($\lambda \sim 1/\eta$; $\eta = \rho_j/\rho_a$). If the wavelength in the counterjet exceeds that in the jet, we infer that the density within the backflowing cocoon is less than the density of the intergalactic medium.

The jet segments J1 and J2 have reasonably flat spectral indices ($\alpha \approx 0.5$, calculated between 1472 and 2368 MHz) which are typical of jets in FR II sources. The counterjet segment CJ1 has a spectrum that is flat ($\alpha \approx 0.4$) close to the core, but steepens to about $\alpha \approx 1$ away from the core. CJ2 also has a steep spectral index, $\alpha \approx 1$. A steeper spectral index on a receding counterjet side can be due to Doppler effects if the rest-frame spectra steepen with increasing frequency (see, for example, Bridle et al. 1989), but CJ1 exhibits spectral steepening over its length and this would require significant changes in jet direction over this length. We hypothesize that the spectra in the jet and counterjet of 0319 − 454 are intrinsically different.

Within the optical extent of the parent galaxy, the counterjet side is significantly brighter than the jet side, while, further from the core, the jet is systematically brighter. When the

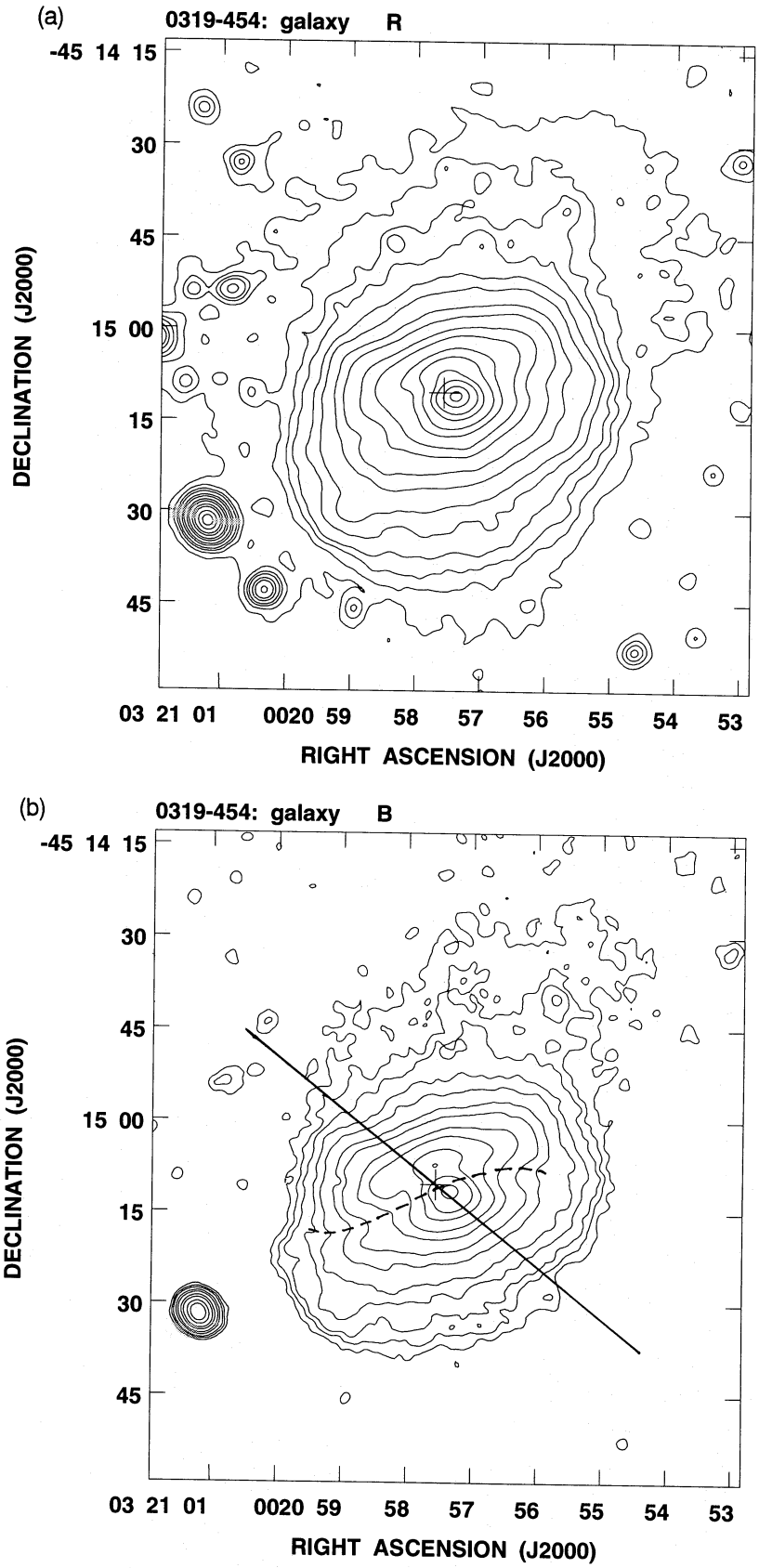

Figure 6. Optical images of the host galaxy with a resolution of 3-arcsec FWHM and a pixel size of 0.4 arcsec. (a) *R*-band image with contours at 15 count pixel^{-1} × (1, 2, 3, 4, 6, 8, 12, 16, 24, 32, 48, 64, 96, 128, 192, 256). (b) *B*-band image with contours at 2.5 count pixel^{-1} × (4, 6, 8, 12, 16, 24, 32, 48, 64, 96, 128, 192). The inner radio axis is indicated by the straight line at a position angle of 51°, and the dust lane by the dashed line. The cross shown in (a) and (b) indicates the position of the peak of the radio core emission. (c) Ratio of pixel intensities in *R*- and *B*-band images shown as superposition of grey-scales in the range 2.5 to 5.5 and contours at 0.1 × (30, 34, 38, 42, 46, 50, 54).

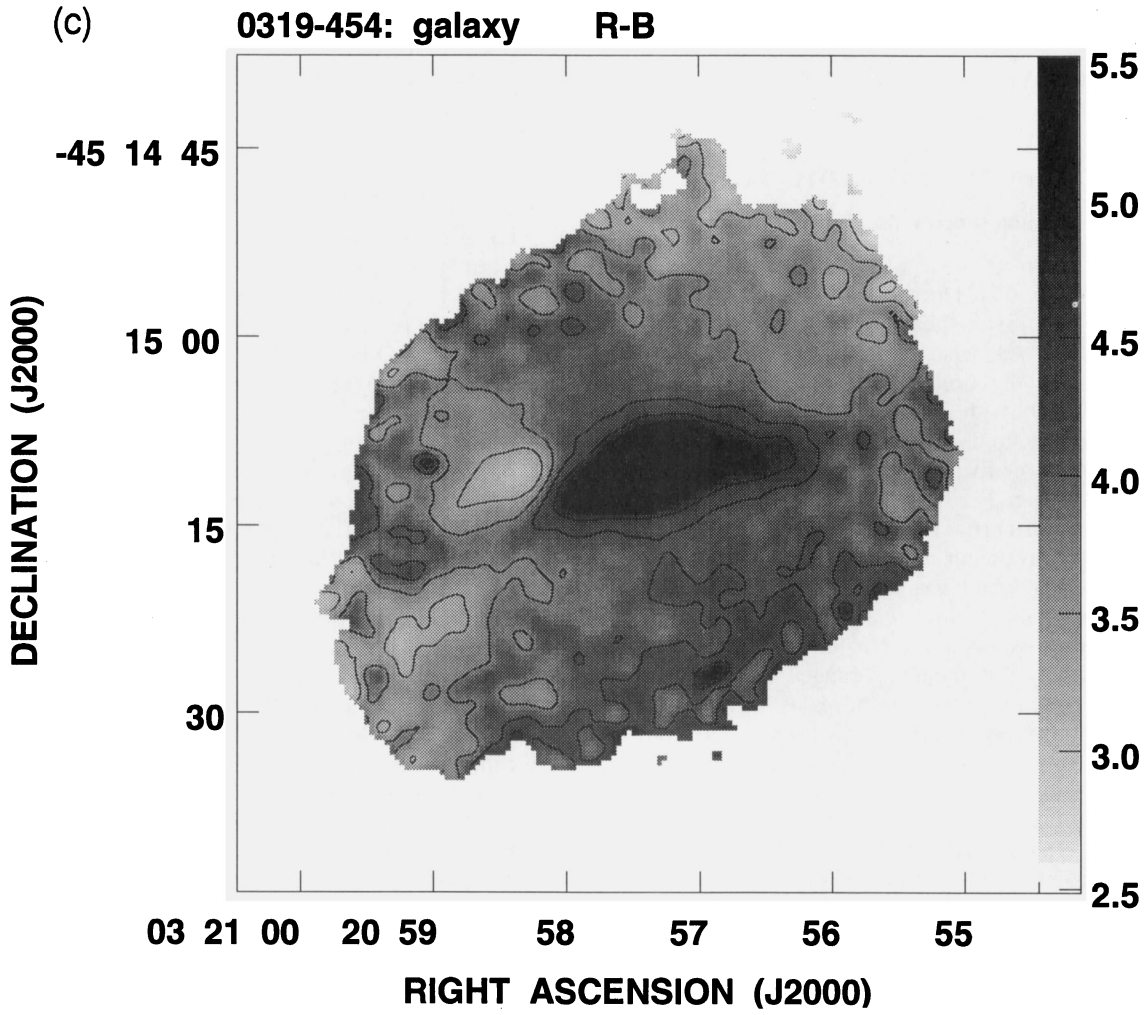

Figure 6 – *continued*

Table 1. Some observed parameters for the core.

Positions (J2000):	RA	DEC
Radio core	03 20 57.55	−45 15 10.1
R-band peak	03 20 57.38	−45 15 10.9
Core flux densities:	**Freq. (GHz)**	**Flux density (mJy)**
	1.5	17.3
	2.4	15.7
	4.8	15.0

counterjet image is rotated through 180° and overlaid on the jet, CJ1 fills the gap between the core and J1, but further from the core there is no filling in of the gaps of one jet by knots of the other jet, as would be expected in the case of alternate or flip-flop ejection. Moreover, the interknot regions are not always devoid of emission. These properties of the jets in 0319−454 are very similar to those of Cygnus A (Carilli 1989).

The normal to the dust lane is inclined away from the sky plane on the NE side, indicating that, if the inner radio axis is orthogonal to the disc, the jet is directed away from the observer and the counterjet is towards the observer. The large (34°) misalignment on the sky plane between the normal to the dust lane and the inner radio axis nevertheless suggests that in 0319−454 the radio ejection axis is *not* orthogonal to the observed disc. Integrated over the same length, the jet and counterjet have a flux density ratio of 3.7, and this could be due to Doppler beaming effects alone if $\beta_j \sin\theta_j > 0.44$, where β_j is the ratio of the velocity of the emitting material to the speed of light, and θ_j is the angle between the ejection axis and the sky plane, although the differences in the spectral indices of the knots on the jet and counterjet sides suggest intrinsic emission differences. The visibility of the beams in 0319−454 may be predominantly decided by their interaction with the environments: backflowing lobe material to the NE and the intergalactic medium to the SW. Bridle (1986) proposed that the core power is probably a better indicator of jet sidedness, and two-sided jets (with jet-to-counterjet ratios of less than 4) generally appear in sources with 5-GHz core powers less than about 1.3×10^{24} W Hz^{-1}. The core power in 0319−454 is a factor of 5 below this dividing line, and the jet-to-counterjet intensity ratio is 3.7. These properties are consistent with the

trends noted by Bridle, and indicate that the presence of the counterjet in 0319−454 is not unexpected. The cause of the counterjet visibility in 0319−454 may therefore not be atypical.

5 THE HOTSPOTS AND RADIO LOBES

5.1 Morphology and spectral properties

Five emission peaks are observed at the extreme end of the NE lobe of 0319−454. Hotspots in FR II radio lobes are normally single emission peaks: double hotspots are also occasionally observed, whereas lobes with more than two hotspots are virtually non-existent (Lonsdale & Barthel 1986; Perley 1989), with 3C 227 and 3C 403 (Black et al. 1992) being rare examples of three hotspots in a radio lobe. The occurrence of five hotspots in the NE lobe of 0319−454 (see Fig. 3) is therefore exceptional, and could indicate extreme properties in the beam generating the structure or in the environment that influences their dissipation. In contrast, the SW lobe has a single bright hotspot (marked SHS). It is important to note that our detection of such a large number of hotspots in the NE lobe is not the result of extreme sensitivity or dynamic range: the hotspots in 0319−454 are seen in 2.4-GHz images with dynamic range as low as 50 and rms noise at the 1-mJy level.

The five hotspot components in the NE lobe have similar peak intensities at both 1.5 and 2.4 GHz, spanning a small range of only a factor of 2.5. HS2 is the brightest, with the hotspots HS3, HS4 and HS5 that lie in a chain towards the north being progressively diminished in brightness at these frequencies. Spectral indices (between 1.5 and 2.4 GHz) for the embedded hotspot components were estimated from peak flux densities obtained by imaging the data with the same resolution and subtracting a baseline fit to the surrounding lobe emission. The most recessed hotspot, HS1, has the flattest spectral index of 0.7. HS5 is slightly steeper ($\alpha = 0.8$) and the remaining hotspots HS2, HS3 and HS4 have spectral indices of $\alpha = 0.9$. The 4.8-GHz observation (Fig. 3) also indicates that HS1 has a much flatter spectral index (between 2.4 and 4.8 GHz). The hotspot in the SW lobe (marked SHS in Fig. 5) is at least five times brighter than any of the hotspots in the NE lobe and also has a flatter spectral index of $\alpha = 0.6$. The secondary emission peak (marked SHS2) in this SW lobe is extended and has a steep spectral index of about 0.9. All six compact hotspots in 0319−454 seem to be marginally resolved in our AT images, and we estimate their intrinsic angular sizes to be roughly 10 arcsec (17 kpc), with HS1 marginally more compact than the others.

The NE lobe has fine-scale filamentary features (Fig. 2b) embedded in the amorphous structure. The spectral index distribution over the NE lobe (computed between 1.5 and 2.4 GHz) is shown in Fig. 7. Surprisingly, most of the lobe has a spectral index very similar to that of the secondary hotspots HS2 to HS4. Upstream, the backflow towards the core is steeper; this is as expected in standard models for FR II sources, where the backflow represents older synchrotron plasma. We derive spectral indices $\alpha \approx 0.9$ in the lobe in the vicinity of the hotspots and $\alpha \gtrsim 1.5$ upstream, although these values are strictly upper limits because of the missing flux density in the 2.4-GHz image.

Curiously, there is a resolved component (marked F in Fig. 7) with a flat spectral index of 0.5 at the centre of the lobe that does not coincide with any emission feature on the total-intensity image. This component is also not identifiable with any galaxy in our COSMOS scan of the sky region (see Section 5.3).

5.2 Formation hypothesis

The primary hotspots in FR II radio galaxies are the ones currently being fed by the beam. These are generally compact ($\lesssim 1$ kpc), are recessed from the lobe edge, have a flat spectral index ($\alpha \lesssim 0.5$), and almost always lie along the source axis. Other secondary hotspots are generally more extended, have steeper spectra, and are predominantly observed (in projection) to lie further from the central engine. We identify HS1 as the primary hotspot in the NE lobe, because it has the flattest spectrum, is observed to have a trail of emission towards the core, and is the most recessed and possibly also the most compact of the five components in the lobe (Fig. 3). We consider the hotspots HS2 to HS5, which have steeper spectra and which are located towards the extreme end of the lobe, to constitute a very unusual connected secondary hotspot structure.

The secondary structure (HS2 to HS5) in the NE lobe does not appear to be a diffuse splatter spot like that seen in 3C 20 (Laing 1989); the secondary hotspots appear to be localized reacceleration sites – individual hotspots – although all four components are embedded in a common emission plateau. HS2 to HS5 may be interpreted as having formed sequentially in this order by a beam with jitter as in Scheuer's dentist-drill model, with the primary hotspot HS1 formed subsequently by a disconnection event (Cox, Gull & Scheuer 1991). The lack of inversion symmetry in hotspots and jet components on the two sides indicates that the jitter is perhaps due to interaction with the environment, rather than precession of the ejection axis. In this picture, HS1 is the current reacceleration site located at the cocoon wall of the NE lobe. The unusual occurrence of multiple secondary hotspots may be either due to continued flow of beam power into the secondary complex structure following disconnection of the beam as it formed the primary, or due to the confinement of the secondary hotspot synchrotron plasma. The similarity in spectral indices between the secondary hotspots and the bulk of the lobe material is indicative of similarities in their ages, and this argues in favour of the latter hypothesis. Since synchrotron brightness diminishes rapidly with expansion, the simultaneous observation of five hotspots in the lobe points towards expansion time-scales much longer than the beam jitter time-scales, and this could be caused by an unusually dense ambient medium in the vicinity of the NE lobe. The greater surface brightness in the NE lobe, as compared to the SW lobe, and its smaller separation from the core, are also consistent with the intergalactic medium being denser to the NE.

The flat-spectrum part of the counterjet component CJ1, located closest to the core, is directed towards the bright and compact hotspot SHS in the SW lobe. The downstream parts of CJ1 and component CJ2, which have steeeper spectra, are directed towards the steep-spectrum extended emission peak (marked SHS2 in Fig. 5) located upstream from SHS. It is possible that SHS is the hotspot that is currently being fed by a straight beam (visible as the flat-spectrum segment of CJ1) from the core, and the rest of the visible counterjet traces the

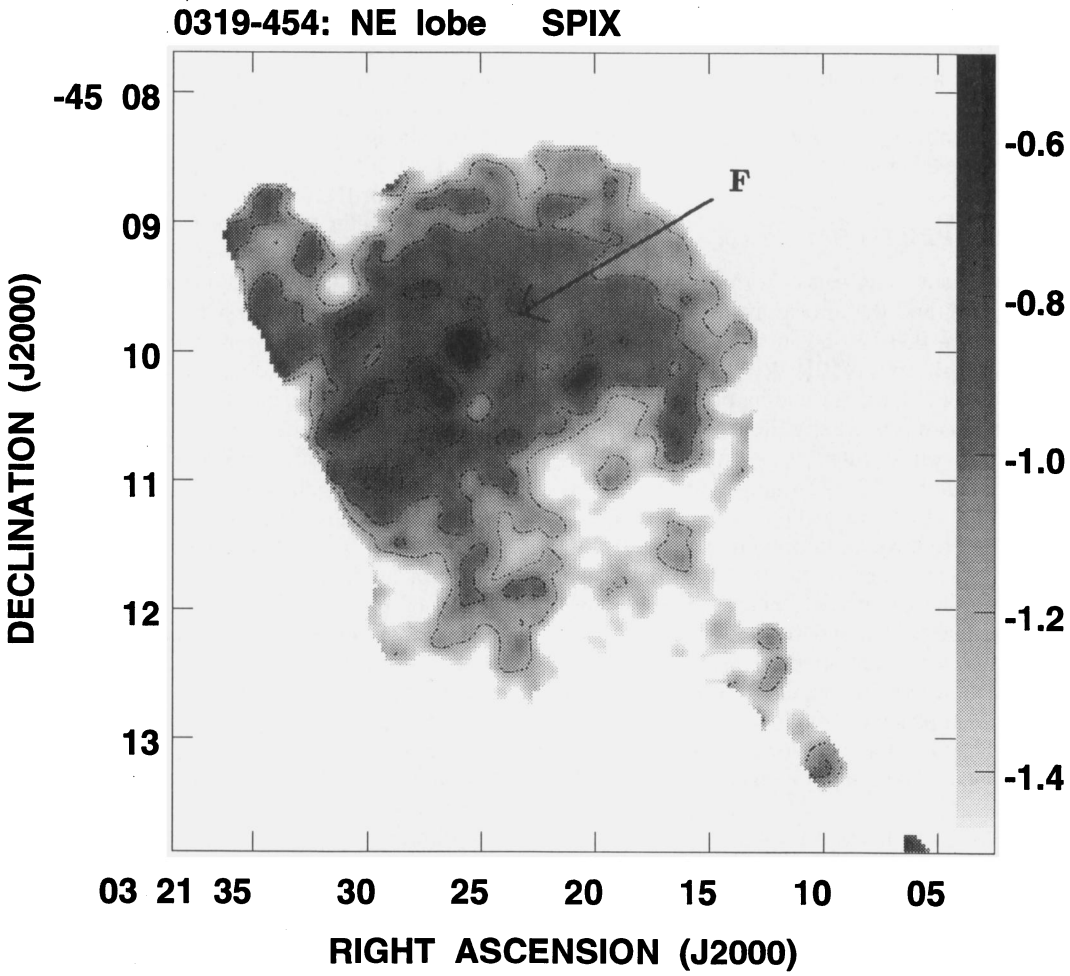

Figure 7. Spectral index distribution over the NE lobe computed between 1.5 and 2.4 GHz. Resolution is 10-arcsec FWHM. Grey-scale range is −1.5 to −0.5, and contours are at 0.1 × (−12, −10, −8, −6). F marks the position of a flat-spectrum region (see Section 5.1).

channel that fed a hotspot at SHS2 in the past. SHS2 is then a secondary hotspot, and a site of past acceleration which expanded and diminished in brightness when the beam ejection direction changed at the core and resulted in a cut-off of the energy injection into the hotspot. Evidence for such a change in the ejection axis in the past may not be so obvious to the NE of the core, because the jet propagation in this direction is likely to be influenced by interaction with the backflow.

The backflow from the NE lobe extends up to the parent galaxy, and appears to flare with extensions to the north and south on reaching the parent galaxy (Fig. 1; Jones 1989). The flaring could be an interaction with any gaseous halo enveloping the parent galaxy, although the flow from the current site of acceleration in the SW lobe appears to be deflected towards the north and does not backflow along the beam axis. The lines joining the core to the two primary hotspots are also not collinear. They make an angle of 2°.2, with the beams from the core appearing to be bent towards the NW. All these could arise from a motion of the parent galaxy with respect to the intergalactic medium in a roughly southern direction. Assuming an upper limit of 500 km s^{-1} for the velocity of the galaxy (which is not a member of a rich cluster), we infer the velocity in the beam to be $< 0.1c$.

5.3 Environment

Inhomogeneity in the ambient intergalactic medium is suggested as the cause of several morphological peculiarities and asymmetries in radio galaxies. If the distribution of field galaxies is a tracer of the intergalactic medium, one expects the galaxy distribution over the source region to display similar inhomogeneity.

We have used the COSMOS southern sky survey database (Yentis et al. 1992) to extract positions and magnitudes of galaxies in the direction of 0319−454; these are plotted in Fig. 1. Galaxies within ±3 mag of the host galaxy, ESO 248-G10, are indicated by the larger cross symbols, and galaxies 3–6 mag fainter are indicated by the smaller cross symbols. The brighter galaxies, with magnitudes close to that of the optical identification for 0319−454, may be expected to lie at approximately the same distance. There is no obvious clustering of these bright galaxies along the radio source axis on either side, and their numbers are too small to measure inhomogeneity on scales corresponding to the radio source extent. Yet there does appear to be some concentration of fainter galaxies within the radio lobe on the NE side of the core as compared to the SW side. Within a band along the radio source axis of width equal to 10 per cent of the

source extent, there are twice as many faint galaxies on the NE side within 1 Mpc of the parent galaxy. Since these faint galaxies may simply be a chance superposition of more distant galaxies, it is not clear that their sky distribution is relevant to the environment of 0319−454, and spectroscopy is needed to settle this issue.

6 DERIVED PROPERTIES

The structure of this giant radio galaxy with prominent hotspots at the extremities, and the appearance and properties of the jets, clearly place 0319−454 in the FR II category. The total radio luminosity is 7×10^{25} W Hz^{-1} at 1.5 GHz, and is above the broad FR I/FR II dividing power suggested by Bridle (1992). In Owen (1993), the FR I/FR II break has been made sharper by considering the dependence on optical luminosity as well, and 0319−454 appears to lie on this dividing line. Therefore this source, like other giant FR II radio galaxies, appears to have a radio luminosity that is low compared with sources in the FR II category, and this could be a consequence of the low particle energy densities and magnetic fields in the giant expanded lobes.

Adopting the standard minimum-energy assumptions (Miley 1980), we have derived the minimum pressures in the amorphous synchrotron plasma in the lobes. Equal energy is assumed in electrons and other relativistic particles, and the filling factor is assumed to be unity for this component. The values of surface brightness were obtained along the four sections marked AA′ to DD′ in the NE lobe (Fig. 2a) and the section marked EE′ in the SW lobe (Fig. 5). Away from the hotspots in the NE lobe, the derived minimum pressures are fairly constant and in the range $6\text{–}9\times10^{-15}$ N m^{-2} in the sections BB′, CC′ and DD′. In the vicinity of the hotspots (AA′), the pressure is about a factor of 2 higher at 19×10^{-15} N m^{-2}. In the SW lobe (EE′), the derived pressure is a factor of 2 lower at 4×10^{-15} N m^{-2}. The lower internal pressure in the SW lobe is again indicative of the external intergalactic medium having a lower pressure to the SW (Subrahmanyan & Saripalli 1993).

The inferred energy density in the NE lobe is about 2×10^{-14} J m^{-3}, and the minimum energy magnetic field has a value of 0.16 nT. The cosmic microwave background radiation (CMBR) has an energy density that is equivalent to a magnetic field of strength 0.45 nT at the redshift of the radio source, so the energy loss in the relativistic electrons of the amorphous synchrotron plasma due to the scattering of CMBR photons will be more important than the energy loss due to synchrotron emission.

We have determined the low-frequency spectral index in the NE lobe by a comparison of our 1472-MHz image with the 843-MHz image of 0319−454 in Jones (1989). In the vicinity of the hotspots, the spectral index is $\alpha=0.7$, and the spectrum steepens to a value of about 1.1 in the backflow mid-way between the hotspots and the core. Assuming the spectral steepening to be due to losses against the CMBR, we have computed the time for the observed spectral evolution to be 9×10^{7} yr and estimate the age of the radio source to be larger by about a factor of 2; the Jaffe & Perola (1973) model for ageing of a synchrotron plasma was adopted, where a single injection of electrons with a power-law initial spectrum and losses independent of pitch angle have been assumed. The total linear extent of the radio source implies an average expansion speed of $0.02c$ for the extremities. This non-relativistic speed suggests that effects of projection and finite light travel time are not responsible for the asymmetry in lobe separations: the asymmetry is intrinsic.

Assuming cylindrical symmetry, the volume in the NE lobe is about 2×10^{66} m^3, and this leads to an estimate of 5×10^{52} J for the total energy in the lobe. This energy is surprisingly similar to that for radio sources of the same class that are an order of magnitude smaller in size and are estimated to have lifetimes an order of magnitude smaller.

Dividing the total energy in the lobe by the source lifetime, we infer the beam power to be 8×10^{36} J s^{-1}. The deconvolved size of the hotspot as well as the width of the observed jets are ≈10 arcsec, and therefore we infer the working surface at the end of the beam to have a radius of 8 kpc and an area of 2×10^{41} m^2. Assuming the estimated momentum in the beam to be balanced in this area by ram pressure of the external medium, we estimate the particle number density in the external medium to be about 0.8 m^{-3}. The advance speed of the hotspot has been assumed to be the expansion speed of the source, although the hotspots are generally believed to travel along the cocoon walls at much higher speeds. If the hotspots advance at $\lesssim0.1c$, the estimate for the density of the external intergalactic medium is at least 10^{-2} m^{-3}, corresponding to a cosmological density parameter $\Omega_{\rm IGM}\gtrsim0.005$. If we assume the beam powers and sizes of the working surfaces on the two sides of the double radio source to be the same, and attribute the differences in the core–lobe separations on the two sides to a factor of 2 difference in the advance velocity of the hotspots, the density of the external intergalactic medium may be inferred to be a factor of 4 higher in the region of the NE lobe as compared with the SW lobe.

7 CONCLUSIONS

Multifrequency radio continuum and optical imaging observations of the radio galaxy 0319−454 have been presented. The powerful radio source is a giant radio galaxy with a very asymmetric edge-brightened FR II structure.

Recent attempts at detecting the elusive counterjets in PRGs have mostly been unsuccessful, and almost all the detections have been single elongated knots (Bridle et al. 1990), many of which do not satisfy Bridle's (1984) criteria for a genuine jet. Cygnus A and 3C 438 are the only FR II sources where we know of the detection of quasi-continuous counterjets. 0319−454 is therefore only the third example of an FR II radio galaxy with a detected counterjet meeting Bridle's criteria.

The jet and counterjet in 0319−454 are both detected over linear distances $\gtrsim400$ kpc. The exceptional lengths probably make these linear structures the longest astrophysical jets known.

The NE lobe of 0319−454 is unusually complex with as many as five compact hotspots and filamentary structure embedded in an amorphous lobe. Twin hotspots are sometimes seen in a single lobe, three hotspot configurations are extremely rare, and we know of no other FR II radio source with as many as five hotspots in a lobe.

These unusual features and the extreme asymmetry in the lobe structure and separation are probably not due to relativistic Doppler beaming effects. Inhomogeneity in the

ambient intergalactic medium over the extent of the radio source, with higher ambient density towards the NE lobe, is probably the cause of the peculiarities.

The parent galaxy is a giant elliptical with a warped dust lane. The galaxy appears to be very disturbed in structure and colour. These peculiarities are probably a consequence of past merger activity.

ACKNOWLEDGMENTS

The authors acknowledge the use of the Australia Telescope Compact Array (operated by the Australia Telescope National Facility) for the radio observations. We thank the staff of the Anglo-Australian Observatory, particularly Gary Da Costa, for the optical CCD images which were provided as service observations. We also thank Ann Burgess for assistance with the COSMOS data extraction, and David Allen, Michael Burton and Vikki Meadows for the IRIS observing and data reduction. LS thanks the Alexander von Humboldt Stiftung for a Postdoctoral fellowship. RWH acknowledges financial support from the Australian Research Council.

REFERENCES

Axon D. J., Unger S. W., Pedlar A., Meurs E. J. A., Whittle D. M., Ward M. J., 1989, Nat, 341, 631
Barthel P. D., 1989, ApJ, 336, 606
Barthel P. D., 1990, in Wagner S. J., Duschl W. J., eds, Physics of Active Galactic Nuclei. Springer-Verlag, Berlin, p. 618
Bertola F., 1987, in de Zeeuw T., ed., Proc. IAU Symp. 127, Structure and Dynamics of Elliptical Galaxies. Reidel, Dordrecht, p. 135
Bertola F., Galletta G., Kotanyi C., Zeilinger W. W., 1988, MNRAS, 234, 733
Bicknell G. V., 1985, Proc. Astron. Soc. Aust., 6, 130
Black A. R. S., Baum S. A., Leahy J. P., Perley R. A., Riley J. M., Scheuer P. A. G., 1992, MNRAS, 256, 186
Bridle A. H., 1984, AJ, 89, 979
Bridle A. H., 1986, Can. J. Phys., 64, 353
Bridle A. H., 1990, in Zensus J. A., Pearson T. J., eds, Parsec-scale Jets. Cambridge Univ. Press, Cambridge, p. 186
Bridle A. H., 1992, NRAO preprint NRAO-91/204
Bridle A. H., Fomalont E. B., Byrd G. G., Valtonen M. J., 1989, AJ, 97, 674
Browne I. W. A., Jackson N., 1990, in Wagner S. J., Duschl W. J., eds, Physics of Active Galactic Nuclei. Springer-Verlag, Berlin, p. 618
Burstein D., Heiles C., 1982, AJ, 87, 1165
Carilli C., 1989, PhD thesis, Massachusetts Institute of Technology
Cox C. I., Gull S. F., Scheuer P. A. J., 1991, MNRAS, 252, 558
Fanaroff B. L., Riley J. M., 1974, MNRAS, 167, 31P
Fernini I., Burns J. O., Bridle A. H., Perley R. A., 1993, AJ, 105, 1690
Hardee P., 1983, ApJ, 269, 94
Heckman T. M. et al., 1986, ApJ, 311, 526
Holmberg E. B., Lamberts A., Schuster H.-J., West R. M., 1978, A&AS, 31, 15
Jaffe W. J., Perola G. C., 1973, A&A, 26, 423
Jones P. A., 1989, Proc. Astron. Soc. Aust., 8, 81
Jones P. A., McAdam W. B., Reynolds J. E., 1994, MNRAS, 268, 602
Knapp G. R., 1987, in de Zeeuw T., ed., Proc. IAU Symp 127, Structure and Dynamics of Elliptical Galaxies. Reidel, Dordrecht, p. 145
Laing R. A., 1989, in Meisenheimer K., Röser H.-J., eds, Hotspots in Extragalactic Radio Sources. Springer-Verlag, Berlin, p. 27
Larson R. B., Tinsley B. M., 1978, ApJ, 219, 46
Leahy J. P., Williams A. G., 1984, MNRAS, 210, 929
Lonsdale C. J., Persson S. E., Matthews K., 1984, ApJ, 287, 95
Lonsdale C. J., Barthel P. D., 1986, AJ, 92, 12
Malin D. F., Carter D., 1980, Nat, 285, 643
Miley G. K., 1980, ARA&A, 18, 165
Owen F., 1993, in Meisenheimer K., Röser H.-J., eds, Jets in Extragalactic Radio Sources. Springer-Verlag, Berlin, p. 273
Perley R. A., 1989, in Meisenheimer K., Röser H.-J., eds, Hotspots in Extragalactic Radio Sources. Springer-Verlag, Berlin, p. 1
Quinn P. J., 1984, ApJ, 279, 596
Rudnick L., Edgar B. K., 1984, ApJ, 279, 74
Sadler E. M., 1987, in de Zeeuw T., ed., Proc. IAU Symp. 127, Structure and Dynamics of Elliptical Galaxies. Reidel, Dordrecht, p. 125
Saripalli L., 1988, PhD thesis, Indian Institute of Science, Bangalore
Saripalli L., Gopal-Krishna, 1987, in Kundt W., ed., Astrophysical Jets and their Engines. Reidel, Dordrecht, p. 247
Saripalli L., Gopal-Krishna, Reich W., Kuhr H., 1986, A&A, 170, 20
Smith E. P., Heckman T. M., 1989, ApJ, 341, 658
Stockton A., 1990, in Wielen R., ed., Dynamics and Interactions of Galaxies. Springer-Verlag, Berlin, p. 440
Subrahmanyan R., Saripalli L., 1993, MNRAS, 260, 908
The Australia Telescope, 1992, Special issue of J. Electr. Electron. Eng. Aust., 12, June
Tonry J. L., 1987, in de Zeeuw T., ed., Proc. IAU Symp. 127, Structure and Dynamics of Elliptical Galaxies. Reidel, Dordrecht, p. 89
Toomre A., Toomre J., 1972, ApJ, 172, 623
Williams A. G., Gull S. F., 1984, Nat, 310, 33
Yentis D. J., Cruddace R. G., Gursky H., Stuart B. V., Wallin J. F., McGillivray H. T., Collins C. A., 1992, in McGillivray H. T., Thomson E. B., eds, Digitised Optical Sky Surveys. Kluwer Dordrecht, p. 67